Earth Planet. Sci. Lett. 662 (2025) 119390

Contents lists available at ScienceDirect

Earth and Planetary Science Letters

journal homepage: www.elsevier.com/locate/epsl

Unraveling remagnetization sources using statistical learning

L.C. Gallo [a,*], M. Domeier [a], P.Y. Antonio [b], F. Sapienza [c], A. Rapalini [d], E. Font [e], T. Adatte [f], R.I.F. Trindade [g], F. Temporim [h], J. Tonti-Filippini [a], P. Silkoset [a], L. Warren [i]

[a] Centre for Planetary Habitability, University of Oslo, Norway
[b] Géosciences Montpellier, Université de Montpellier, France
[c] Department of Statistics, University of California, Berkeley, CA, United States
[d] Consejo Nacional de Investigaciones Científicas y Técnicas, Buenos Aires, Argentina
[e] Departamento de Ciências da Terra, Universidade de Coimbra, Portugal
[f] Institute of Earth Sciences (ISTE), University of Lausanne, Switzerland
[g] Department of Geophysics, University of São Paulo (USP), Brazil
[h] Faculdade de Ciências e Tecnologias, Universidade Federal de Goiás, Brazil
[i] Instituto de Geociências e Ciências Exatas, Departamento de Geologia, Rio Claro (SP), Brazil

ARTICLE INFO

Editor: H. Bao

Keywords:
Paleomagnetism
Machine learning
Remagnetization
Geochemistry
Rock magnetism
Ediacaran

ABSTRACT

The paleomagnetic archive provides invaluable insights into Earth's history, but its records are often obscured by various geological processes. A prime example is remagnetization, which can replace the original natural remanent magnetization. Although magnetic overprints can be detected by traditional paleomagnetic tests, the mechanisms responsible for them often remain elusive because linking bulk magnetic properties to their microscopic sources is inherently challenging. Here, we bridge this gap by pairing an extensive rock magnetic and geochemical dataset with statistical learning techniques for the first time. Using a Random Forest regressor trained on geochemical data, we accurately predict the growth of fine-grained magnetite in an undeformed late Ediacaran section of remagnetized carbonate rocks from Paraguay. Our modeling results identify the K/Al ratio—alongside K and Sr contents—as key predictors of this remagnetization mechanism. Notably, clay mineralogy analyses further link the K/Al ratio to enhanced clay authigenesis (illitization) driven by K-feldspar dissolution and albitization—processes that also release iron. Together, these findings indicate that remagnetization occurred via authigenic magnetite formation under isochemical diagenesis—without the involvement of external fluids. This novel application of statistical learning to uncover the geochemical drivers of chemical remagnetizations provides a robust framework to investigate and understand these events. It could also open new avenues for their direct dating, thereby significantly enriching the global paleomagnetic record.

1. Introduction

Paleomagnetism is integral to unraveling Earth's paleogeographic evolution, as well as understanding the history of the geomagnetic field and the deep Earth processes that power it. However, the utility of the paleomagnetic archive hinges on our ability to accurately assess the age of a magnetic remanence. In the ideal case, a primary remanence is preserved and the age of the magnetization coincides with the formation age of the rock. But rocks can be remagnetized by various means and, although classic field tests can identify remagnetizations (i.e., baked contact test, conglomerate test, and fold test), the underlying mechanisms of remagnetization are often elusive. This uncertainty complicates age determination, rendering $\sim 15-20\%$ of the global paleomagnetic database (GPMDB: Pisarevsky et al., 2022) effectively unusable for paleogeography, yet these data hold significant potential if their origins and ages can be discerned.

One common means of remagnetization occurs through the growth of authigenic magnetic minerals, enabled by the breakdown of pre-existing Fe bearing minerals (e.g., Katz et al., 1998) and/or the introduction of exotic fluids (e.g. Lu et al., 1991). Determining which of these pathways a particular chemical remagnetization followed is challenging, and the mechanism(s) of remagnetization in many instances is unknown or poorly understood (Van Der Voo and Torsvik, 2012). However, chemical remagnetizations may leave distinct geochemical traces,

* Corresponding author.
E-mail address: l.c.gallo@geo.uio.no (L.C. Gallo).

https://doi.org/10.1016/j.epsl.2025.119390
Received 20 January 2025; Received in revised form 25 April 2025; Accepted 26 April 2025
Available online 7 May 2025

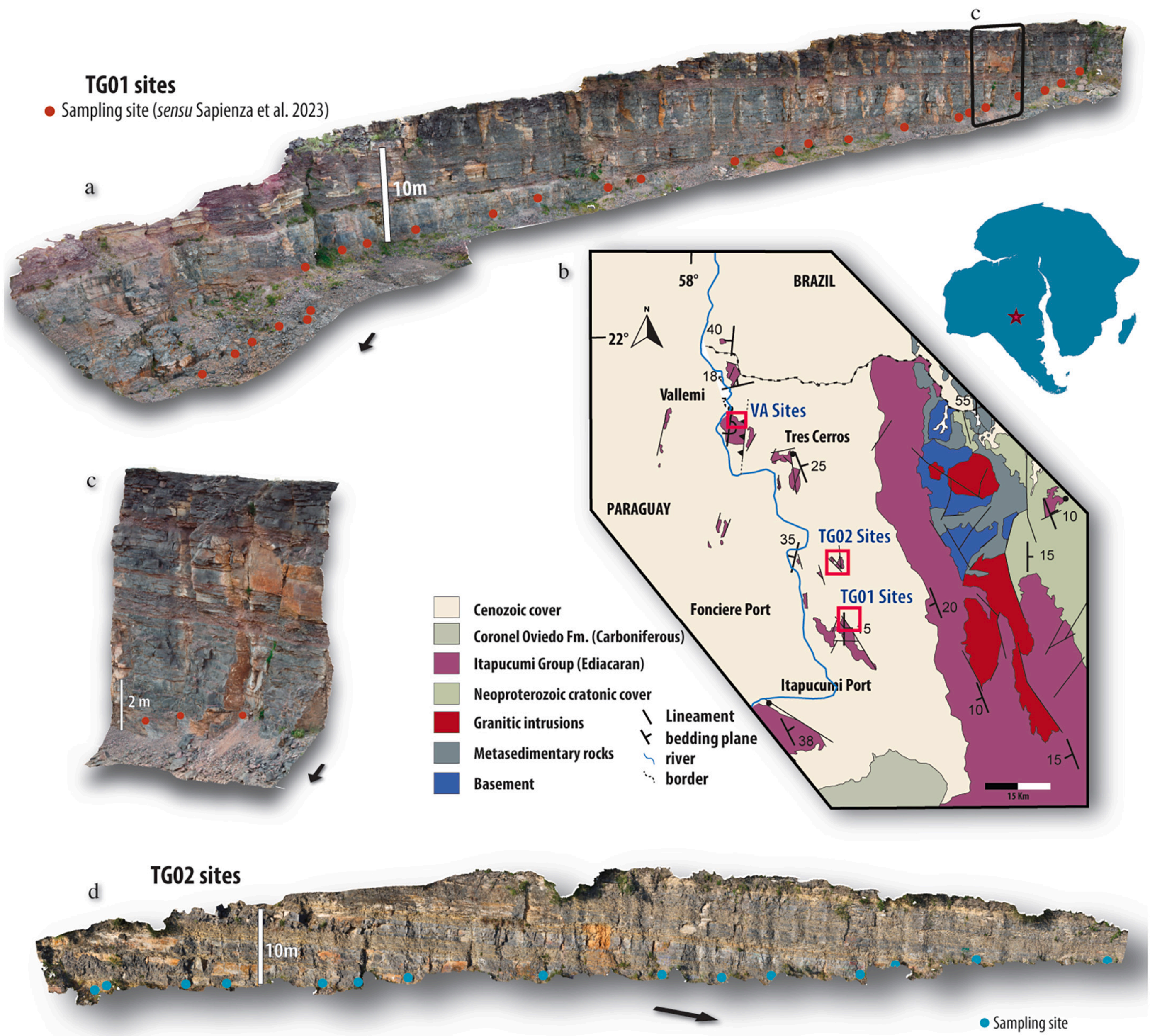

Fig. 1. Digital outcrop models (a, c-d) showing the stratigraphic distribution of samples collected from the studied areas (see Data Availability section for interactive 3D model links). Black arrows indicate the direction of geographic north. b) Schematic geological map of the area around Vallemi, northeast Paraguay, illustrating the spatial distribution of geological units. The location of the area is marked by a red star in the inset map of Gondwana.

although they could be subtle and complex. An untapped opportunity to uncover them lies in the use of statistical learning tools, which are adept at identifying complex and non-linear patterns in big datasets. While recent advancements in machine learning (ML) offer breakthrough potential, the challenges of data acquisition in paleomagnetism make it difficult to generate the large, high-quality datasets that ML requires. As a result, the full potential of ML applied to paleomagnetism remains largely untapped.

In this paper, we explore this opportunity through a joint paleomagnetic-geochemical analysis of a carbonate sedimentary succession spanning the Ediacaran-Cambrian transition in Paraguay (South America). Our analyses reveal that the section has undergone significant remagnetization, which is quantified with rock magnetic measurements. Using a high-resolution geochemical dataset collected alongside the rock magnetic data, we employ a Random Forest regressor trained on the geochemical features extracted from the paleomagnetic samples to accurately predict the extent of the remagnetization. Unlike traditional machine learning methods, which often prioritize predictive accuracy, our statistical learning framework focuses on uncovering the geochemical mechanisms behind remagnetization through feature importance analysis, offering valuable insights and a novel framework for unraveling the complex processes driving remagnetization.

2. Geological background and sampling

The Ediacaran-Cambrian transition, a pivotal but enigmatic interval in Earth's history (Domeier et al., 2023), is recorded in the upper and lower sections of the Tagatiya Guazú and Camba Jhopo formations of the Itapucumi Group in Paraguay. This sedimentary succession was deposited in a tidally influenced mixed carbonate-siliciclastic ramp and is globally renowned for its exceptionally well-preserved Ediacaran fossil assemblage (Warren et al., 2019, 2023). In the western region (Fig. 1), these units exhibit deformation and characteristics of lower greenschist facies (chlorite zone) metamorphism. In contrast, in the eastern part, they comprise a broad, undeformed and unmetamorphosed cover (Warren et al., 2019, 2023).

Two hundred paleomagnetic samples were collected from two sections of the Tagatiya Guazu formation ('TG01' and 'TG02') and one section of the Camba Jhopo formation ('VA'). The bases of sections TG01 and TG02 are ~11 km apart but their structural attitudes are similar and they can be easily correlated based on their vertical facies association and architecture. VA was collected in the slightly deformed area, to obtain samples with a different structural attitude, enabling the application of a regional fold test. Samples were distributed stratigraphically at approximately 0.5 m intervals to maximize the number of sites (Gerritsen et al., 2022; Sapienza et al., 2023). Aerial image acquisition with a drone was used to construct virtual outcrops via Structure from Motion (SfM), with samples precisely located within these models (Fig. 1 a,c,d; see Data Availability section for interactive 3D model links).

3. Experimental results

3.1. Paleomagnetism

We performed stepwise alternating field (AF) and/or thermal demagnetization on all recovered paleomagnetic specimens ($N = 181$) collected from the TG01 and TG02 sections, measuring their remanence with a 2G Enterprises DC-SQUID Superconducting Rock Magnetometer at the University of Oslo. The VA samples were measured in 1996 at the University of Buenos Aires, but have been re-analyzed and are first reported herein. Samples were frequently prone to alteration and magnetic grain growth during heating, resulting in the acquisition of spurious components. To mitigate this effect, AF demagnetization was conducted up to 140 mT in 5 mT increments, followed by thermal demagnetization up to 660 °C in 20 to 40 °C steps. To remove the effects of low-temperature oxidation and weathering, several samples were first thermally demagnetized at 150 °C and then subjected to stepwise AF demagnetization (Van Velzen and Zijderveld, 1995). The directions of magnetic remanence were determined using principal component analysis (Kirschvink, 1980), without forcing the final magnetization components to pass to the origin (Heslop and Roberts, 2016). On average, the samples exhibit very low natural remanent magnetization (NRM) intensities. Section TG01 has a mean mass-normalized NRM of 3.04×10^{-7} Am^2/kg, which is slightly higher than that of section TG02, with a mean of 1.84×10^{-7} Am^2/kg.

Progressive demagnetization first removed a randomly directed viscous component, after which continued AF demagnetization revealed a medium-coercivity component ("A") that unblocked above 30 mT. This component, with a relative contribution to the total NRM of between 4% in TG01 and 11% in TG02, exhibits linear decay in Zijderveld diagrams, either to the origin (Fig. 2 d,e) or transitioning to a higher-coercivity component that remains unaffected by AF demagnetization (Fig. 2 a,b,c). Although it constitutes only a small fraction of the NRM, this component is well-defined, yielding fits with a maximum angular deviation (MAD) median value of 8.9° over 5 to 19 steps. Together, they define a mean direction of $D = 10.7°$, $I = 31.7°$ ($n = 133$, $A_{95} = 3.45°$, $\kappa = 13.5$) in geographic coordinates and $D = 6.4°$, $I = 34.9°$($n = 133$, $A_{95} = 4.13°$, $\kappa = 9.8$) after tilt correction (Fig. 2h). A complete listing of all individual component directions, along with their respective demagnetization steps and statistical parameters, is provided in Supplementary Table S1. The bootstrapped fold test (Tauxe and Watson, 1994) clearly indicates the secondary nature of this component (Supplementary Fig. S1). Directions, when transformed into virtual geomagnetic poles (VGPs) plot close to other poles associated with a widespread remagnetization event in West Gondwana around ~ 480 Ma (Donardelli Bellon et al., 2024; Font et al., 2006; Pescarini et al., 2024; Trindade et al., 2004), although they do not overlap. As shown below, we nevertheless interpret this to represent a similarly-aged remagnetization. A new paleomagnetic pole 'Tagatiya' can be computed from these VGPs (Fig. 2j, pole longitude = 317.6 °E, pole latitude = 48.5 °N, $A_{95} = 3°$, $N = 133$, circular standard deviation = 19.8°).

The percentage of magnetic remanence retained after AF demagnetization varied from 66% in TG01 to 15% in TG02 (Fig. 2f). Thermal demagnetization was performed on samples retaining more than ~ 20% of their NRM after AF treatment. This enabled the isolation of a distinct high-temperature component ("B") unblocking between ~ 320 °C and ~ 700 °C in 42 samples (Fig. 2g). This component, which displays dual polarity, is likely hosted by hematite due to its high coercivity, maximum unblocking temperature, and origin-trending direction. The bootstrapped fold test supports the secondary nature of this component (Supplementary Fig. S1, Tauxe and Watson, 1994). Its corresponding VGPs (Fig. 2i, pole longitude = 40.2 °E, pole latitude = −86.3 °N, $A_{95} = 3.4°$, $N = 42$, circular standard deviation = 12.2°) is statistically indistinguishable from that of mid-Cretaceous stable south America (Somoza and Zaffarana, 2008) (Supplementary Fig. S2).

3.2. Rock magnetism

Rock magnetic experiments across the stratigraphic sections confirm the presence of a mixture of high- and low-coercivity phases, which align with the previously described components of remanence. Using a Quantum Design Magnetic Properties Measurement System (MPMS3) at the University of Montpellier, low-temperature characterization was performed by cooling samples to 20 K, either in a 2.5T magnetic field (field-cooled, FC) or without a field (zero-field-cooled, ZFC), followed by the application of a low-temperature saturation isothermal remanent magnetization (LTSIRM) at 20 K and then measuring the remanence upon warming to 300 K. Although the Verwey transition is often suppressed in carbonates due to low-temperature oxidation (Jackson and Swanson-Hysell, 2012), some ZFC-LTSIRM curves still exhibit this transition (Fig. 3a), confirming the presence of magnetite.

As the samples were warmed to room temperature, approximately 50% of the remanence was lost (Fig. 3a), suggesting that a significant portion of the ferromagnetic phase is superparamagnetic at room temperature and does not contribute to the NRM. The presence of such a superparamagnetic (SP) to single-domain (SD) grain-size fraction has been proposed to constitute a 'fingerprint' of remagnetization (Jackson and Swanson-Hysell, 2012). The separation between FC-LTSIRM and ZFC-LTSIRM curves (Supplementary Fig. S3) further suggests a contribution from goethite (Liu et al., 2006). In addition, samples were imparted a room-temperature SIRM at 2.5T and measured in zero field during cooling to 20 K and subsequent warming to 300 K. In some samples (TG02.4 and TG02.29), a remanence "hump" is observed between 150 K and 200 K (Fig. 3b), a hallmark of maghemitization, or low-temperature oxidation of magnetite (Özdemir and Dunlop, 2010). An inflection in the remanence during cooling around 225 K is clearly visible (Fig. 3b, Supplementary Fig. S3) and is associated with the Morin transition of fine-grained hematite (Özdemir and Dunlop, 2014).

Hysteresis loops and backfield curves were measured on 52 samples with a Lake Shore PMC MicroMag 3900 Vibrating Sample Magnetometer (VSM) revealing a strong diamagnetic contribution from the carbonate matrix, with over 90% of samples displaying a dominant diamagnetic response at high fields (Supplementary Table S2). We use the high-field slope of the hysteresis loops (high-field susceptibility, X_{hf}) to estimate the relative contributions of the diamagnetic + paramagnetic and ferromagnetic phases to the overall magnetic susceptibility. Hysteresis loops reveal that the maximum applied field of 1.5 T did not approach the reversible regime for most samples (Fig. 3c,d and Supplementary Fig. S4). This response is likely due to high-coercivity phases such as goethite or hematite. Thus, hysteresis parameters Hc, Mrs and Ms are non-saturation estimates (Özdemir and Dunlop, 2014). Despite known limitations—particularly the difficulty of distinguishing magnetic phases due to incomplete saturation—the samples plot within the Day diagram in a region generally associated with mixtures of su-

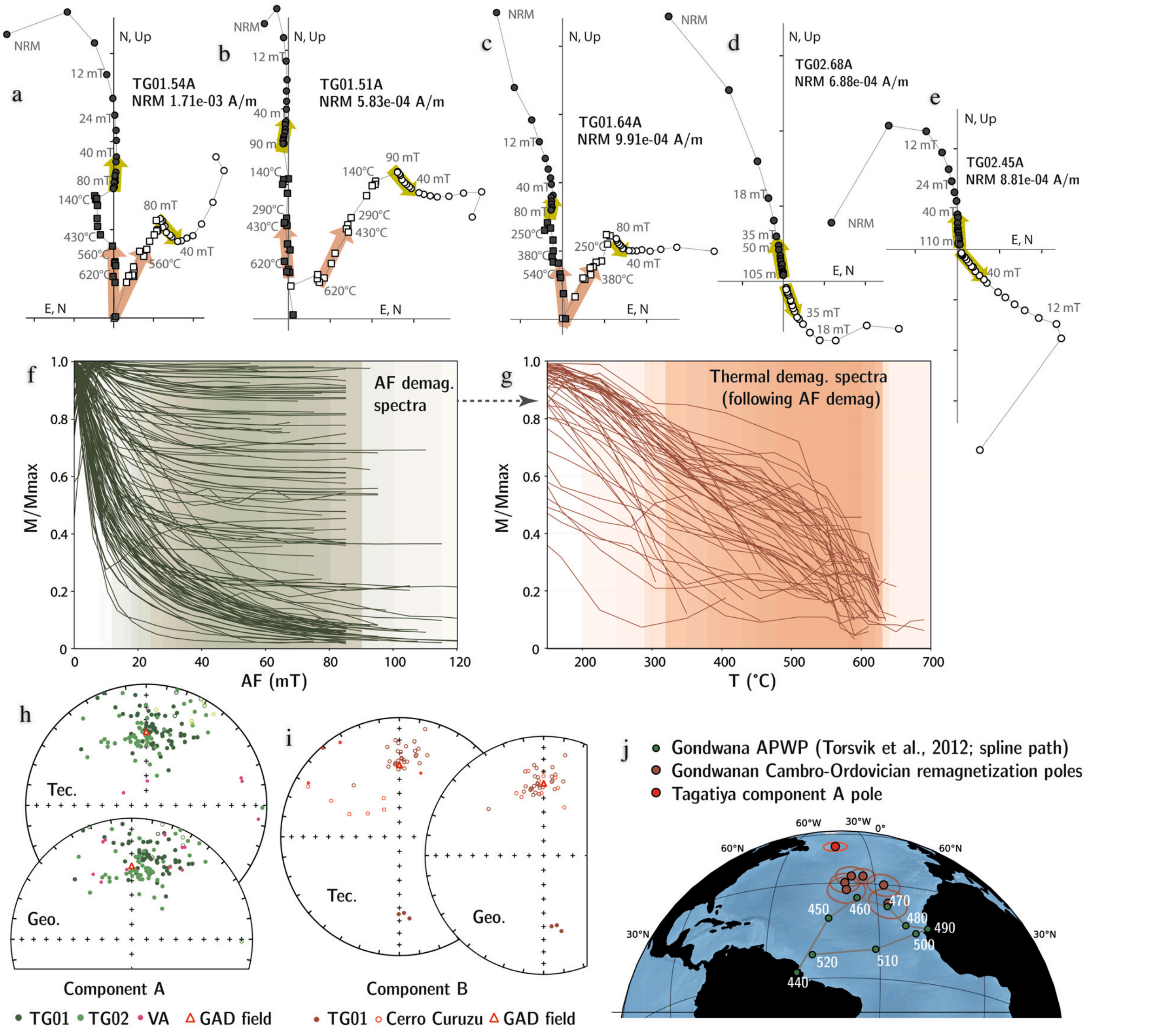

Fig. 2. Summary of paleomagnetic results. a-e) Example orthogonal vector diagrams of stepwise AF (circles) and thermal (squares) demagnetization results. Solid/open symbols represent horizontal/vertical projections. Green/red arrows highlight component A/B fits. f-g) AF and thermal demagnetization spectra. In (f) and (g), the temperature (field) range over which components were isolated is marked for each sample, and the zones of higher intensity indicate the most frequent temperature (field) ranges. h-i) Directions associated with component A and B in geographic ('Geo.') and tilt-corrected ('Tec.') coordinates; solid/open symbols denote positive/negative inclinations. j) Position of the Tagatiya component A paleopole with respect to the Gondwanan APWP of Torsvik et al. (2012) and other Gondwanan poles inferred to represent Cambro-Ordovician remagnetizations.

perparamagnetic (SP) and single-domain (SD) ferrimagnets (Fig. 3e). Following the high-field slope correction, the appearance of constricted ("wasp-waisted") hysteresis loops dominate the samples (Fig. 3c) and suggests that the main magnetic carrier is likely magnetite with different grain sizes. However, rectangular hysteresis loops are also seen (Fig. 3d), consistent with the presence of antiferromagnetic material. First order reversal curves (FORCs) generally exhibit a narrow central ridge, consistent with the presence of SD grains, but in some samples PSD-like behavior is also observed. FORC distributions are often concentrated near the origin and exhibit a vertical spreading along the Bu axis, a hallmark of SP grains (Roberts et al., 2014). Magnetic mineral unmixing was performed on the backfield curves to further characterize and separate coercivity components (Maxbauer et al., 2016). This revealed two distinct phases, with each component displaying a variable relative contribution to the total measured magnetization (Fig. 4a,b). The lower-coercivity component, with a mean of $\sim$ 85 mT, is consistent with magnetite and is present in all the samples (Fig. 4a). In contrast, the high-coercivity component, with a mean coercivity of 863 mT, corresponds to hematite (Fig. 4c; Supplementary Table S2). A few samples also exhibited evidence for a minor higher coercivity phase ($> 1T$) that could reflect the presence of goethite (Supplementary Table S1).

Stepwise thermal demagnetization of three orthogonal IRMs (Lowrie, 1990) with decreasing fields of $1.12T$, 700 mT, and 100 mT, confirms the presence of magnetite in the low-coercivity fraction, showing unblocking temperatures around $\sim 560\,°$C (Fig. 4d). The medium-coercivity component decays gradually up to $\sim 450\,°$C, consistent with maghemite.

A dominant SP-SD grain-size population, which is widely used as an indicator of diagenetic/authigenic magnetite growth (Jackson and Swanson-Hysell, 2012; Dearing et al., 1996), is confirmed in our samples by the drop in ZFC-LTSIRM and FC-LTSIRM upon warming. However, the SP content can be further constrained in either the frequency or time domain. We measured the viscous remanent magnetization (VRM) decay of a 500 mT IRM as a proxy for SP content using a J-meter coercivity spectrometer (Enkin et al., 2007). The remanent magnetization decreases over time due to the thermal relaxation of magnetic grains with short relaxation times, following a logarithmic time relationship (Dunlop, 1973) that can be described by a power law, $a \cdot t^{-b}$, where a

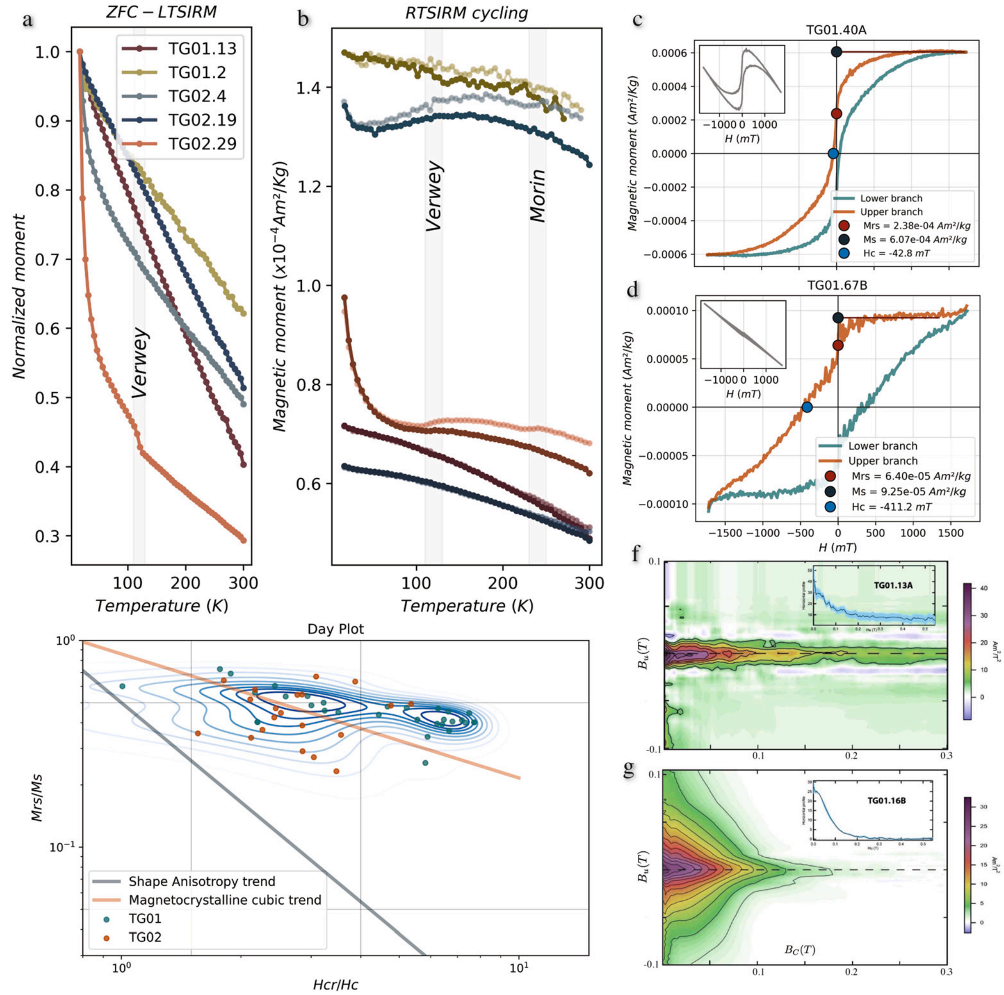

Fig. 3. Summary of rock magnetic results. The reader is referred to Fig. S3 for a detailed breakdown of the low-temperature curves. a) Remanence during warming of a low-temperature SIRM following zero-field cooling to 20 K. b) Cycling of a room temperature SIRM down to 20 K and then back to 300 K. c-d) Hysteresis loops after slope correction (uncorrected loops shown in insets) showing wasp-waisted (c) and more square-like (d) behavior. e) Day plot of the summary hysteresis parameters compared with theoretical trends (Jackson, 1990). f-g) First-order reversal curve (FORC) diagrams showing SD (f) and PSD (g) behavior; insets display the horizontal profile at $B_u = 0$.

is the initial signal and b is an exponent approaching -1 and roughly proportional to SP content (Fig. 4e). In general, the samples exhibit significant viscous decay, with $6 - -21\%$ of the IRM at 500 mT being lost within 100 seconds (Fig. 4e, Supplementary Fig. S5). In the frequency domain, SP content can be assessed from the decrease in magnetic susceptibility with an increase in the measuring field frequency (Dearing et al., 1996). Here, we conducted five measurement series on 183 samples using a AGICO Kappabridge (MFK1-FA) at 976 Hz and 15,616 Hz (Fig. 4f). Several parameters are commonly used to evaluate frequency-dependent susceptibility, with $X_{FD} = 100(X_{LF} - X_{HF})/X_{LF}$ being among the most widely applied. However, it is important to note that the diamagnetic contribution in these rocks is substantial (as indicated by the negative susceptibility values in Fig. 4f) due to their high carbonate content. Consequently, the normalization by X_{LF} makes this parameter highly sensitive to the carbonate content. To reduce this dependency, we instead use $X_{FV} = X_{LF} - X_{HF}$, which minimizes the impact of carbonate and more directly reflects SP content. A strong correlation—as demonstrated by Pearson correlation coefficients and highly significant p-values—is observed between the X_{FV} parameter and the remanence carried by the A component, evaluated as the amount of NRM remanence lost within the selected alternating field demagnetization range for the A component (Fig. 4g). This indicates that the A component, predominantly carried by magnetite linked to the SP-SD fraction, can be quantified effectively through the frequency-dependent susceptibility parameter X_{FV}.

In summary, rock magnetic experiments indicate that the A component, which aligns with the direction of other Gondwanan remagnetizations, is carried by fine-grained magnetite, a significant portion of which is superparamagnetic at room temperature. Notably, the pervasiveness of this remagnetization can be assessed through the frequency-dependent susceptibility parameter X_{FV}, as shown by its strong correlation with the mass normalized NRM of this component. The B component is consistent with fine-grained or pigmentary hematite with a broad unblocking temperature range (Collinson, 1974). Goethite may also be present in some specimens, but it does not contribute to the isolate components. Finally, although we observed no behavior diagnostic of pyrrhotite, its presence cannot be ruled out, and the breakdown of pyrite, which commonly alters upon heating, could explain the erratic behavior of some specimens during thermal demagnetization beyond $\sim 350\,^{\circ}$C.

3.3. Compositional analysis

3.3.1. XRD on whole-rock and clay mineralogy

A subset of 10 samples were selected for whole-rock and clay mineralogy characterization by X-ray diffraction (XRD) using a Thermo Scientific ARL X-TRA diffractometer at the ISTE-University of Lausanne

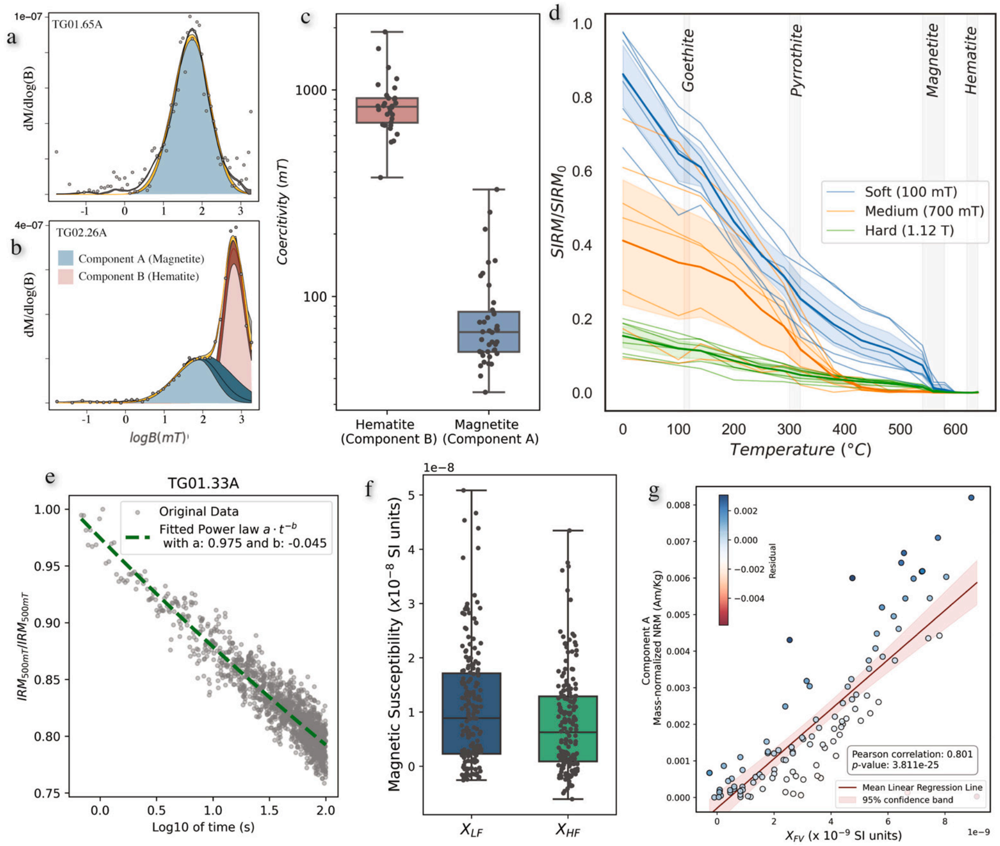

Fig. 4. Summary of rock magnetic results. a-b) Examples of coercivity unmixing analysis showing one (a) or two (b) components of coercivity. c) Boxplot showing coercivity (mT) distributions estimated for the low (magnetite) and high (hematite) coercivity components distinguished from IRM unmixing analysis (as shown in panels a-b). The box limits represent the interquartile range (IQR) with the lower and upper bounds marking the 25th and 75th percentiles, respectively. d) Thermal demagnetization of three orthogonal IRMs (Lowrie, 1990). Thin lines represent individual sample results, while the thick lines show the mean result. The shaded areas indicate the 95% confidence intervals of the mean, calculated through bootstrapping. The expected maximum unblocking temperature intervals of several phases are highlighted by gray bands. e) Viscous decay of a 500 mT IRM as repeatedly measured by a J-meter coercivity spectrometer over 100 s; note time is presented on a log-scale. f) Measured magnetic susceptibilities at low (976 Hz) and high (15,616 Hz) frequency; individual data shown as points and the corresponding distributions are shown as box-and-whisker plots. g) Sample-based comparison of the amount of NRM remanence lost (within the selected alternating field demagnetization range) for the A component against frequency-dependent magnetic susceptibility.

(Switzerland), following the methods described in Adatte et al. (1996). Semi-quantitative analyses using XRD peak intensities were referenced to external standards. Clay characterization was determined on oriented slides of decarbonated samples and concentrated clay suspensions were separated into $2-16$ µm and <2 µm size fractions by centrifugation. Clay mineral peak positions (2θ angle; Moore and Reynolds, 1989) were identified on diffractograms of ethylene-glycolated samples for the <2 µm granulometric fraction (Fig. 5a).

The bulk mineralogical composition of the studied samples is more than $\sim 95\%$ calcite, between $0.4-4.1\%$ quartz and less than 1.2% phyllosilicates (Supplementary Table S3). The coarse fraction of clay minerals (2-16 mm) is dominantly illite ($60-92\%$) with lesser amounts of chlorite ($6-29\%$) and kaolinite ($2-22\%$). K-feldspar, plagioclase and goethite are present in low concentration (noted in Supplementary Table S4 as count per second). The finer clay mineral fractions (<2 µm) contain illite ($32-65\%$), chlorite ($2-22\%$), kaolinite ($1-13\%$), illite-vermiculite mixed-layers ($0-26\%$), and illite-smectite mixed-layers ($12-28\%$) (Supplementary Table S5). The illite crystallinity index, the so-called Kübler index (Kubler, 1967), calculated for the <2 µm fraction, varies between 0.22 and 0.44, indicating anchizone conditions, with paleotemperatures potentially reaching but not exceeding $\sim 200\,°C$ (~ 6.5 km burial depth considering a geothermal gradient of 30 °C/km). Illite-smectite mixed-layers layers are recognized in both TG01 and TG02 samples. The smectite content of each mixed-layer clay was estimated and we distinguish two types (Fig. 5a): those exhibiting less than 20% swelling (R1 ordering) and those exhibiting more than 20% swelling (R0 ordering). The average smectite content of the R1 fraction is $\sim 10\%$, whereas for R0 it is $\sim 31\%$. Because these mixed-layer clays represent intermediate phases in the progressive transformation of smectite to illite ('illitization'), we use the $R1/R0$ ratio as an illitization proxy, where larger values reflect a smaller proportion of smectite and thus a more advanced degree of illitization (*i.e.* dissolution of smectite and its subsequent precipitation as illite).

3.3.2. *Energy Dispersive X-ray Fluorescence (XRF)*

172 polished rock sub-samples were analyzed for major and trace elemental composition with a Bruker S1 Titan 800 portable XRF (pXRF) under controlled laboratory conditions (see Supplementary Text S1 for comprehensive technical details on instrument settings). The application of pXRF proved invaluable in enabling the acquisition of a sufficiently large dataset, which would be onerous to obtain with conventional analytical methods. This extensive dataset provided the foundation for robust statistical geochemical analyses. For validation, the composition of ten duplicate bulk samples was also determined via XRF on glass pellets with a PANalytical Axios spectrometer (see Supplementary Text S1, Supplementary Table S6). The validated measurements demonstrated a median % error of 2.25 (Supplementary Figure S8) and a median value R^2 of 0.94 (Supplementary Figure S7), underscoring both the reliability and accuracy of the resulting elemental concentrations. Consistent with XRD results, the CaO values from bulk-rock pXRF show an interquar-

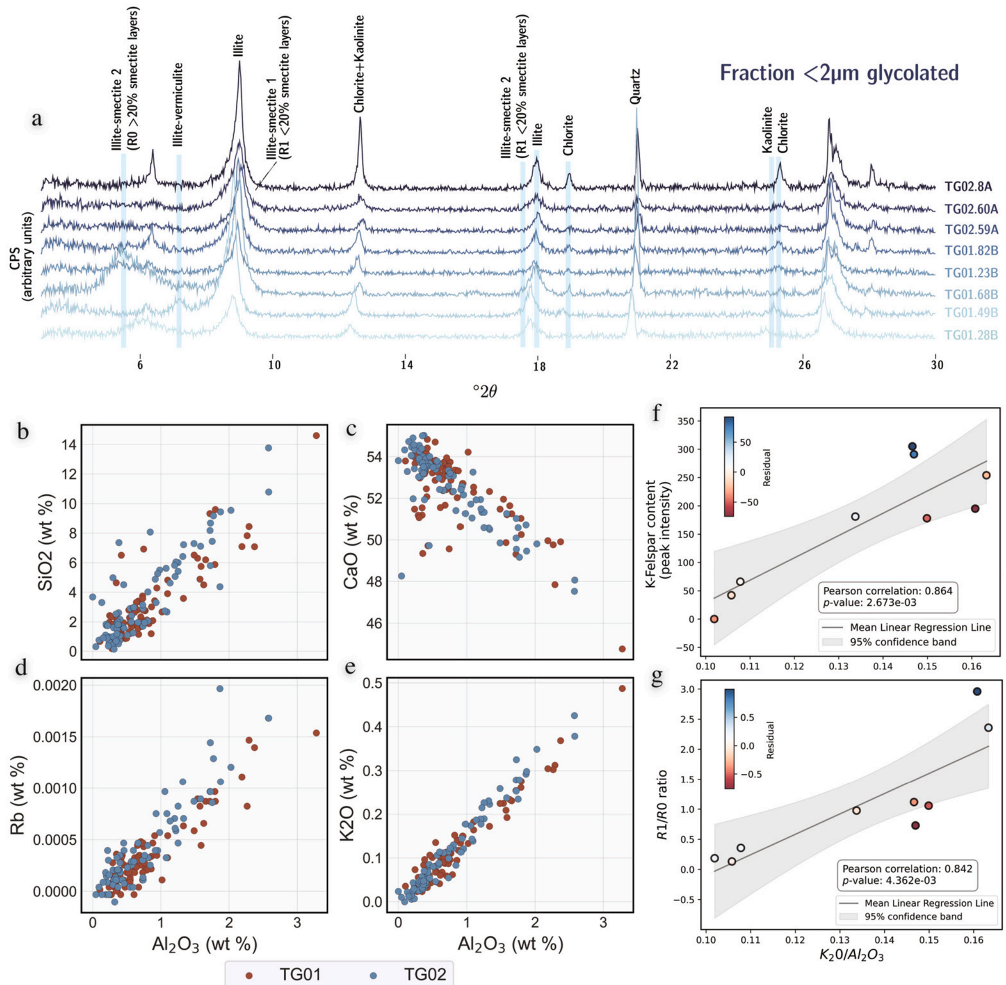

Fig. 5. Summary of compositional analysis. a) X-ray diffraction (XRD) patterns of the < 2 µm glycolated clay fraction for representative samples. Major clay mineral peaks, as well as quartz reflections, are labeled. b–e) Geochemical plots of oxide (CaO, SiO_2, K_2O) and trace element (Rb) concentrations versus Al_2O_3 (all in $wt\%$). f) Correlation between K-feldspar peak intensity (from XRD) and Al_2O_3, showing a Pearson correlation coefficient of 0.97 ($p = 3.16 \times 10^{-4}$). The solid line denotes the mean linear regression fit. g) Relationship between $R1/R0$ (degree of illitization) and the ratio K_2O/Al_2O_3, with a Pearson correlation coefficient of 0.834 ($p = 2.69 \times 10^{-3}$). The residuals from the linear regression are color-coded, and the fitted line represents the mean trend with its confidence intervals.

tile range (IQR) between 51.3% and 53.7% (n = 172), suggesting that the samples are nearly pure calcite. The geochemistry is primarily influenced by the relative proportion of siliciclastic to carbonate material, as elevated CaO levels are associated with lower SiO_2 and Al_2O_3 contents (Fig. 5b) and so yield positive correlations among the non-carbonate components, which include SiO_2, Al_2O_3, K_2O, TiO_2 and Rb. However, the particularly strong correlation between K and Al suggest that K is not mobile but may be associated with small amounts of clay or detrital minerals within the carbonate matrix (Fig. 5d). Rb, which is often less mobile during weathering, also shows a correlation with K, indicating its retention in minor detrital clays resistant to diagenetic alteration (Bayon et al., 2022). The K/Al ratios, with an interquartile range (IQR) between 0.18 and 0.25 ($n = 172$), align closely with values observed in river clays (Bayon et al., 2021). Together, these correlations likely reflect the stability and retention of K and Rb in clay minerals rather than significant post-depositional metasomatic alteration or chemical weathering. Additionally, the samples show high concentrations of Sr (IQR between 1293 – 2579 ppm), typical of marine carbonates. These values are consistent with those reported by Warren et al. (2019) for carbonates of the Tagatiya Guazu Formation, which are interpreted as primary. Other geochemical proxies further support the absence of post-depositional alteration (*i.e.*, fluid percolation or weathering), including the lack of $\delta^{13}C$ and $\delta^{18}O$ covariance and low Mn/Sr and Mg/Ca ratios (Warren et al., 2019).

Because the transformation of smectite to illite is contingent upon the availability of K as a reactant (Meunier and Velde, 2013), the K/Al ratio can be a useful proxy for assessing the extent of illitization (van de Kamp, 2016). Notably, Fig. 5g demonstrates a clear relationship between the $R1/R0$ ratio and the K/Al ratio in the studied samples, suggesting that the availability of K was a limiting factor in the illitization process. This K availability appears to be controlled by variations in detrital content rather than later metasomatic additions, as evidenced by the strong correlation between the K/Al ratio and the K-feldspar content (Fig. 5h).

3.3.3. *Scanning Electron Microscopy (SEM) and Energy Dispersive X-ray (EDS) mapping*

Sub-samples of intact paleomagnetic cores were prepared for SEM imaging and mineral mapping using standard techniques on a Hitachi SU5000 FE-SEM field emission scanning electron microscope equipped with a dual Bruker Quantax XFlash 30 EDS system at the University of Oslo. In combination with SEM imaging, EDS mapping enabled us to examine the mineralogical compositions at the microscale, allowing for the identification and detailed characterization of various mineral phases and their distribution, including those with high Fe content (Fig. 6a). One prominent phase, identified as hematite (probably secondary, see Section 5.2), is observed filling cavities as interlocking meshworks of subhedral to euhedral crystals of generally < 1 µm size, which we refer

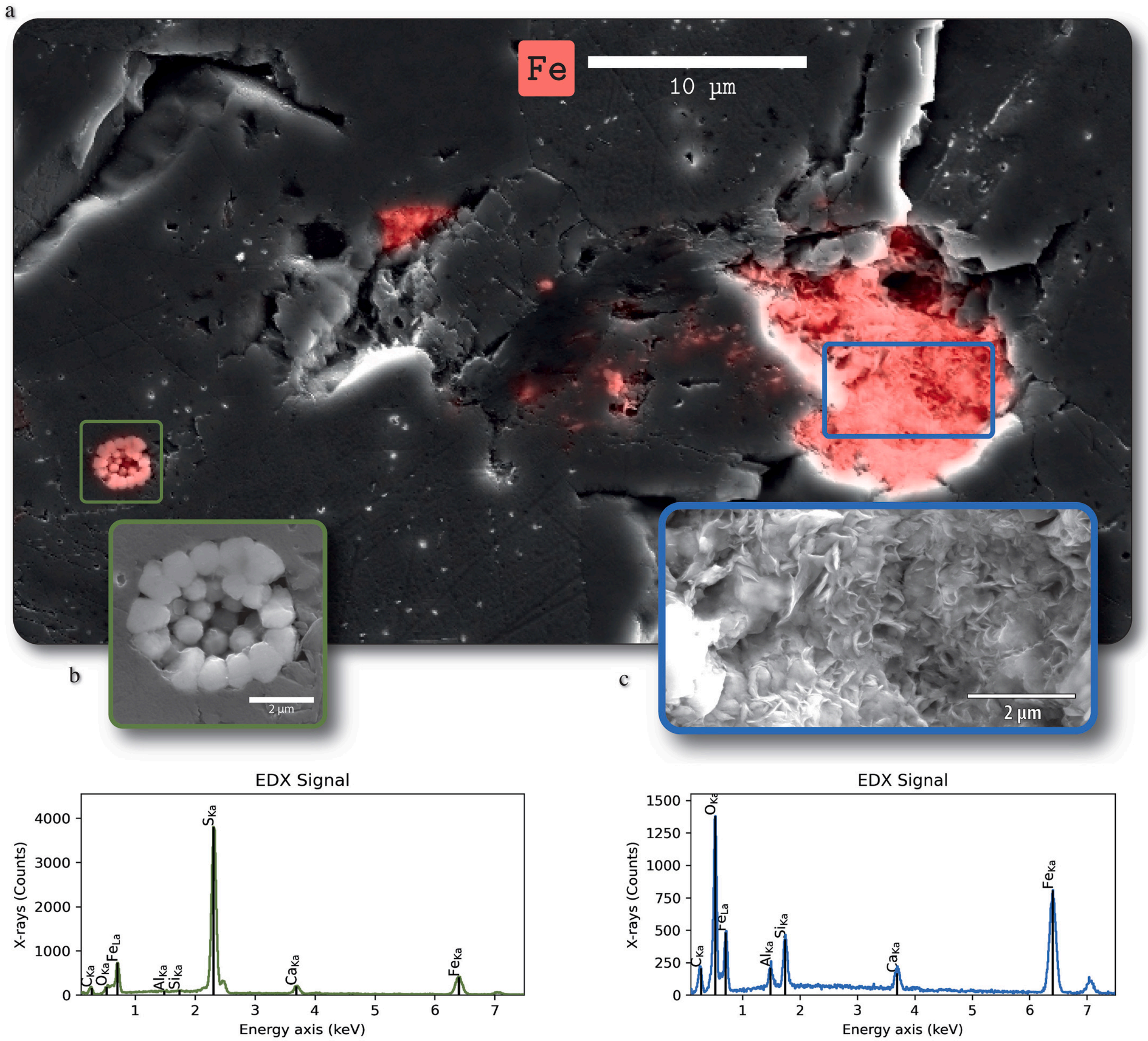

Fig. 6. SEM backscattered electron images. a) SEM image with an overlay of EDS map highlighting Fe-rich areas. b) Framboidal pyrite alongside its corresponding EDS spectrum, confirming the elemental composition dominated by Fe and S. c). Microcrystalline hematite filling cavities as interlocking meshworks of subhedral to euhedral crystals of < 1 μm size. Amounts of silicon (Si), and aluminum (Al) can be ascribed to a clay coating and calcium (Ca) to the background carbonate matrix.

to as microcrystalline hematite (Walker et al., 1981). Framboidal pyrite was also identified (Fig. 6). The Fe/S ratios of eight framboidal sulfides were analyzed using an Electron Microprobe Cameca SX100. Fe/S atomic ratios consistently yielded a value of ~ 0.49, confirming the chemical composition of stoichiometric pyrite without any evidence of a pyrrhotite mixture (Supplementary Fig. S6). No magnetite was observed in the SEM analyses, likely because the dominantly SP-SD population, as characterized by rock magnetism, has few if any grains exceeding $\sim 30nm$—and so they are too small to be resolved by SEM.

We processed EDS elemental maps and automate the identification of detrital grain boundaries using the Python library HyperSpy (de la Peña et al., 2017). This is achievable because the detrital grains are embedded in a carbonate matrix, creating sharp compositional gradients. The watershed segmentation (Beucher and Meyer, 2018) was applied to a gradient map generated after summing the Al and Si elemental maps, which highlights regions often associated with detrital grains (Fig. 7b). By simulating a flooding process on the gradient map and treating it like a topographic surface, the algorithm effectively delineates regions corresponding to individual grains, with high compositional differences acting as ridges that separate them. This method effectively segmented the detrital fraction and revealed its spatial association with areas of elevated Fe content, which may indicate the presence of Fe-bearing minerals (Fig. 7c). Notably, regions with Fe concentrations above background levels strongly correlate with the detrital fraction, particularly in elongated, clay-like structures. Albitization of K-feldspar is commonly observed and may have provided a source of K for illitization in these rocks. An important observation is the consistent presence of pyrite within the matrix, entirely unassociated with the detrital fraction (Fig. 7d). During early diagenesis, microbial respiration fueled by organic matter could consume oxygen and Fe oxides, resulting in the dissolution of detrital magnetite and/or hematite and the formation of paramagnetic pyrite (Roberts et al., 2013).

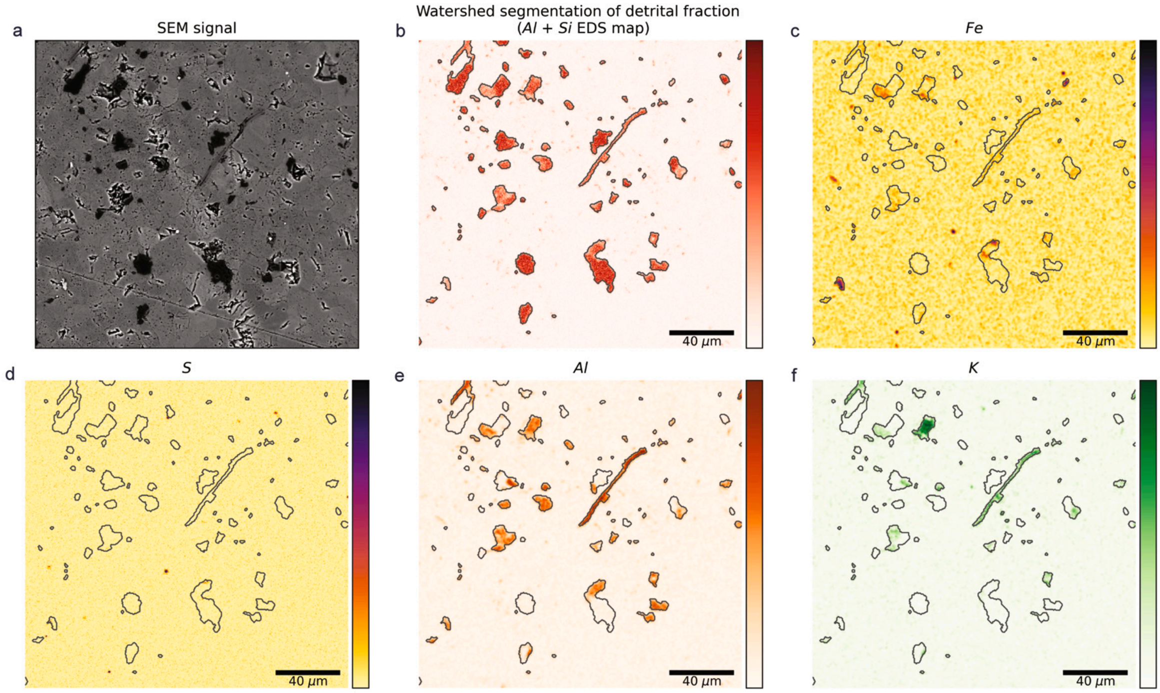

Fig. 7. Automated identification of detrital grains via EDS elemental mapping and Watershed segmentation (Beucher and Meyer, 2018). a) SEM image showing darker detrital grains embedded within a lighter carbonate matrix. b) Result of applying the watershed algorithm on compositional gradients (derived from the EDS maps), highlighting segmented detrital grains in red. Elemental distribution maps for Fe (c), S (d), Al (e), and K (f), with the watershed boundaries overlaid in black. The sharp compositional transitions between detrital grains and the surrounding carbonate allow the watershed algorithm to delineate individual grains. Elevated Fe signals in several segmented regions are closely associated to the detrital fraction.

4. Random forest regression

In recent years, machine learning (ML) algorithms have become an invaluable tool for uncovering hidden patterns and relationships in scientific datasets. However, the challenges of data acquisition in paleomagnetism often hinder the generation of the large, high-quality datasets required for ML. In this work, we have constructed a dataset consisting of 182 measurements of X_{FV} as the target variable—that is, the variable we aim to predict in order to better understand its behavior. This important step forward in collecting larger datasets was possible due to the fact that frequency-dependent susceptibility X_{FV} tracks the strength of the A component that is held by authigenic SP-SD magnetite (Fig. 5g). In addition to X_{FV}, the same samples were analyzed for major and trace elemental compositions using a pXRF analyzer (see Section 3.3.2). With these geochemical data, we aimed to quantify any potential relationships between element concentrations and the degree of remagnetization, as assessed by the magnitude of X_{FV}. Beyond elemental concentrations, elemental ratios were included to enhance the model's predictive capacity and interpretability. Ratios such as K/Al, K/Rb, Ti/Al, Rb/Sr, Ca/Al, Fe/S, and Si/Al carry important information about geological processes and environmental conditions, enabling the inference of diagenesis, weathering, provenance, or depositional environment. A summary of the dataset is provided in Supplementary Table S7.

We thus seek to develop a statistical model that quantifies the degree of remagnetization (evaluated as the magnitude of X_{FV}) to illuminate any underlying relationships between element concentrations and remagnetization. To this end, we employed a Random Forest (RF) regressor to analyze the data. A random forest regressor is a statistical method that combines small decision trees to achieve better accuracy, a strategy known as bagging (Breiman, 2001). These decision trees, which form the foundational elements of the model, are supervised algorithms that recursively partition the data based on optimal feature splits, capturing complex, non-linear relationships in a tree-like structure. RF was chosen due to its robust performance on small to medium-sized tabular datasets (Grinsztajn et al., 2022) and its interpretability, as it provides feature importance scores that highlight the variables most relevant for prediction. Additionally, its structure inherently reduces the impact of multicollinearity, as the random selection of feature subsets during tree construction minimizes the effects of highly correlated predictors. Moreover, we expanded our analysis by testing several algorithms—including multiple linear regression, ridge regression, lasso regression, decision trees, k-nearest neighbors (kNN), and support vector machines (SVM). Our results indicated that Random Forest consistently delivered the best performance, while SVM also demonstrated good performance (Supplementary Fig. S9).

Given the observations in the feature matrix and to avoid overfitting while ensuring robust performance evaluation, we partitioned the dataset into training (80%) and test (20%) sets. The test set serves as a proxy for how well the model performs on unseen data, providing an unbiased measure of its generalizability. Hyperparameter tuning of the number of trees, maximum depth, and minimum samples per split was performed exclusively on the training data using 4-fold cross-validation–the training set was divided into 4 shuffled subsets, the model trained on three and tested on the fourth in turn–while sampling 10000 different parameter combinations and selecting the combination that minimized absolute error. The model achieved a R^2 score of 0.8273 in the training set and 0.6120 on the test set (i.e., unseen data), indicating that it explains 83% of the variance in X_{FV} on the training set and 60% on the test set, thereby demonstrating a high level of predictive accuracy (Fig. 8a).

Feature importance was evaluated using Shapely Additive Explanation (SHAP) values, which quantify the average marginal contribution of each feature to the model's predictions (Lundberg, 2017). This approach enabled us to interpret the model's results and identify the most influential variables driving the prediction of the frequency-dependent susceptibility X_{FV}. The feature importance results from the Random Forest model indicate that K, Sr, and the K/Al ratio are the most significant predictors of X_{FV} (Fig. 8b). These findings underscore the critical role of the smectite-to-illite transformation, as the K/Al ratio is

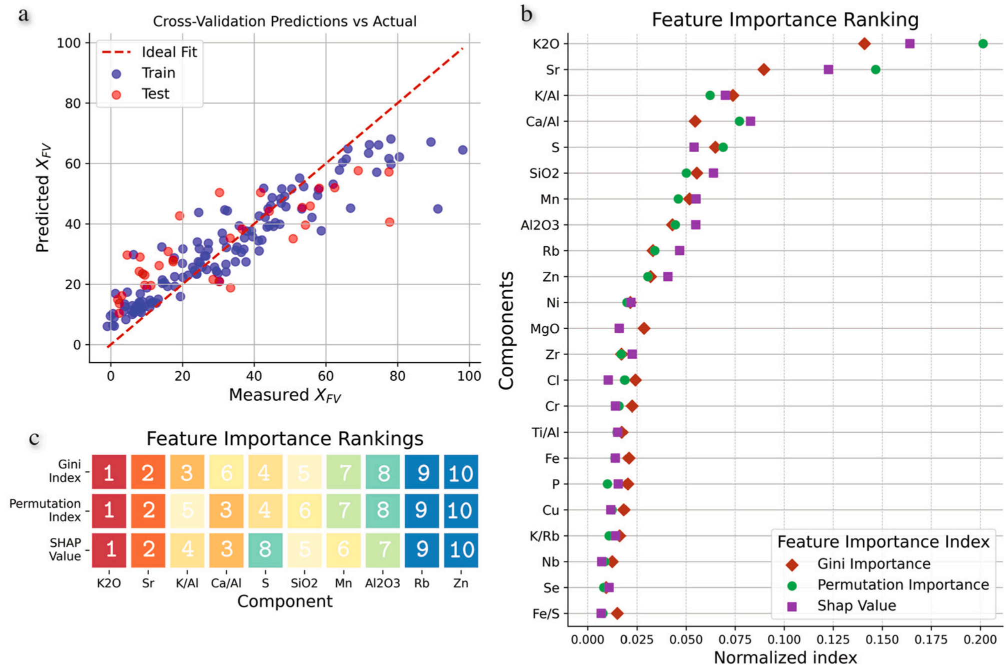

Fig. 8. Random Forest regression results for predicting frequency-dependent susceptibility (X_{FV}) using geochemical data. a) Scatter plot of the predicted versus observed X_{FV} for the training and test datasets, illustrating model performance (the red dashed line is the 1:1 reference). b) Comparison of feature importance metrics (Gini, permutation, and SHAP) highlighting the most influential elements and elemental ratios for X_{FV} prediction. c) Ranked feature importance across the top variables, with color scales indicating the order of importance under each metric.

a well-established proxy for illitization (van de Kamp, 2016). Alternative feature importance methods, including permutation tests and mutual information criteria, yielded results consistent with those derived from SHAP values (Fig. 8c). Although the size of our dataset is relatively small for typical data science applications, it is substantial within the context of paleomagnetic studies. Taken together, these results confirm a robust and consistent identification of the key features responsible for predicting the magnitude of X_{FV}.

5. Discussion

Our results demonstrate that the Ediacaran Itapucumi Group in Paraguay has been pervasively remagnetized. From the stepwise demagnetization of its NRM, we have identified two magnetic components: a likely Cambro-Ordovician component (component A) associated with magnetite, and a Cretaceous or more recent component (component B) associated with hematite. Rock magnetic experiments conducted across temperature, time, and frequency domains have characterized the magnetite as a population of superparamagnetic (SP) to stable single-domain (SSD) grains. These grains, which formed as secondary chemical precipitates, can be quantified using frequency-dependent magnetic susceptibility measurements, along with their remanent contribution to the NRM. A parallel series of compositional analyses reveals no evidence of post-depositional rock alteration–such as metasomatic processes–and shows that the geochemistry of the detrital fraction aligns with the geochemical fingerprints of modern river clays, characterized by $K/Rb < 240$, $K/Al < 0.42$, and $Rb/Al < 0.0022$ (Bayon et al., 2021).

5.1. *Role of illitization in remagnetizations and the origin of component A*

The transformation of detrital smectite to illite, first proposed several decades ago as a remagnetization mechanism (Jackson et al., 1988; McCabe et al., 1989; Lu et al., 1991; Katz et al., 1998), leads to the release of Fe (Boles and Franks, 1979), enabling the formation of authigenic Fe-oxides, and thus the acquisition of a chemical remanent magnetization (CRM). However, key questions remain about the underlying drivers of illitization, which bear on the ultimate trigger and timing of CRM acquisition. Illitization requires both thermal energy and a source of K as a reactant. Because illitization begins at shallow burial depths and temperatures from 70 °C (Hoffman and Hower, 1979), the process is ultimately limited by the availability of K necessary for the transformation of the precursor clay into illite (Hower et al., 1976). Accordingly, one model to explain regional remagnetization episodes invokes the introduction of K-rich basinal brines, transmitted across a broad area in association with orogeny (Oliver, 1986). This model has been applied to explain widespread late Paleozoic remagnetization across eastern and central North America in association with Alleghanian orogenesis (Jackson et al., 1988; Lu et al., 1991), based on the correlation between authigenic magnetite concentration and authigenic illite, K-Feldspar and quartz (e.g., Lu et al., 1991; McCabe et al., 1989). In contrast to the exotic fluid model, an isochemical illitization process (proceeding in a geochemically closed system) could be viable where there is sufficient free K already available, a condition commonly associated with the dissolution of K-rich tuffs, K-feldspars, and micaceous minerals (Meunier and Velde, 2013; Hower et al., 1976). The in situ albitization of K-feldspar during burial diagenesis (Saigal et al., 1988) can serve as a source of K, promoting illitization and the release of Fe necessary for the growth of authigenic magnetite. This coupled process of illitization and authigenic magnetite growth could potentially occur over a wide area via regional sedimentary burial.

Our findings strongly indicate that authigenic magnetite growth was driven by Fe release during illitization within a geochemically closed system. By applying statistical learning to a high-resolution geochemical dataset collected alongside rock magnetic data, we identified the most important parameters for predicting the strength of magnetite-hosted remagnetization. These include K content, Rb, Sr, and the K/Al ratio. Notably, the K/Al ratios are correlated with the $R1/R0$ ratio–an indicator of the degree of illitization–and also show a strong association with the content of K-feldspar. Rb, closely associated with K and enriched in K-bearing minerals (Bayon et al., 2022), plays a key role in the trained model, suggesting that the K required was likely sourced from detrital K-feldspar. SEM observations further reveal frequent albitization of K-feldspar, underscoring its role as a localized K source. This direct link between K-feldspar albitization and illitization highlights that the process was limited by the local availability of K derived from K-feldspar albitization, rather than by the supply of K from an external source. If both detrital smectite and sufficient quantities of K-feldspar were available in these carbonates, the only additional ingredient needed to drive illitization would have been heat, provided by sedimentary burial. In this context, the Cambro-Ordovician age inferred for component A (determined from a comparison of the pole position to the reference apparent polar wander path) is not unreasonable, given that final Gondwana assembly is thought to have continued into the Cambrian with metamorphic illites from the Paraguai belt along the southern margin of the Amazonia Craton having yielded $^{40}Ar/^{39}Ar$ ages of 496 – 484 Ma (Tohver et al., 2010). Regional sedimentary burial associated with orogenesis could have thus provided the thermal impetus needed to trigger (or significantly accelerate) the illitization process and authigenic magnetite formation. Ultimately, magnetite growth would have been arrested when the supply of Fe waned, which would have occurred when one or more of the reactants driving clay diagenesis (K-feldspar, smectite and heat) was exhausted.

A remaining question is whether the A component is dominantly a CRM acquired during initial burial (when the authigenic magnetites first grew through the critical volume necessary to lock in a stable remanence), or a thermoviscous remanent magnetization (TVRM) that was progressively acquired after burial until the temperature was reduced by regional exhumation (Donardelli Bellon et al., 2024; Kent, 1985). Because magnetic relaxation time increases exponentially as temperature decreases, the laboratory unblocking temperature spectra of a component can be used to assess the likelihood of it representing a TVRM for a given temperature history (Dunlop and Özdemir, 1993). Unfortunately, alteration during thermal demagnetization has precluded a detailed resolution of the thermal stability spectra of component A, but given its AF demagnetization spectra and the assembled rock magnetic evidence, we assume this component is held by SD magnetite that—being authigenic—is probably stoichiometric. Component A is thus expected to have a high thermal stability, with a maximum unblocking temperature close to the Curie point of magnetite (580 °C). According the Kübler Index, the Tagatiya Guazú carbonates did not experience burial temperatures beyond 200 °C. Following Pullaiah et al. (1975), a TVRM acquired at this temperature over a few 10's of Myr should have a maximum unblocking temperature of ~ 400 °C, significantly lower than the Curie point of magnetite. We thus prefer the interpretation that component A is primarily a CRM, although we cannot exclude the possibility that a similarly aged partial TVRM has been acquired alongside this CRM. Further work to isolate the thermal stability spectra of component A could shed additional light on this matter.

5.2. Origin of hematite remagnetization (component ‘B’)

The paleomagnetic pole calculated from the high-temperature (B) component is statistically indistinguishable from that of mid-Cretaceous stable South America (Somoza and Zaffarana, 2008). At the start of the Cretaceous, the opening of the Atlantic Ocean triggered extensive denudation along its margins (Gernon et al., 2024). Thermal history models across the region support this, indicating near-continuous exhumation since the Early Cretaceous.

The component's broad unblocking spectra, along with our SEM observations of microcrystalline hematite, suggest hematite formation during low-temperature (< 200 °C) oxidation of dissolved Fe-oxides (e.g. ilmenite, titanomagnetite or magnetite) or Fe-bearing grains (e.g. biotite, pyrite or other Fe-bearing carbonates). Syn-tectonic hematite growth is frequently observed during orogenic uplift and we attribute this to a gradual shifting of redox conditions towards more oxidative environments, presumably due to gravity-driven infiltration of surface water (Rasmussen and Muhling, 2019). This time-dependent, redox-driven alteration aligns with the dual polarity observed in this component, supporting a Cretaceous overprint with dual polarity linked to oxidative changes as exhumation advanced along the Atlantic margin.

5.3. Fate of original NRM

Organic matter is susceptible to microbial degradation, which, in sulfide-rich environments, consumes oxygen and generates sulfides at the expense of Fe-oxide dissolution (Roberts et al., 2013). This process has been observed in carbonate environments, where microbial activity has been shown to erase the original magnetization through the dissolution of Fe-oxides and the formation of sulfides (e.g., Huang et al., 2019; Tarduno, 1992). Descriptions of organic matter in other nearby Neoproterozoic basins (*e.g.*, Font et al., 2006) make this scenario plausible for these rocks, highlighting that microbial facies and Ediacaran fossil content are commonly found throughout the Tagatiya Guazu Formation (Warren et al., 2019). This process likely led to the complete removal of the original NRM. SEM imaging and EDS mapping reveal framboidal pyrites within the matrix that are completely isolated from other detrital grains, suggesting they were originally part of the detrital fraction; this observation supports the idea that pyrite formed through the dissolution of primary Fe-oxides.

5.4. Broader implications

Our study establishes a novel framework to uncover the geochemical drivers of chemical remagnetizations, providing new insights into these events and enhancing our ability to understand them. Through pinpointing the key geochemical patterns associated with remagnetization, we may also identify additional mineral phases associated with these processes, potentially including phases that can be directly dated (*e.g.*, Brenner et al., 2022). In turn, the ability to accurately determine the age of remagnetizations would be transformative, in enabling a much broader utilization of the global paleomagnetic archive.

Earlier studies utilized the Ar/Ar isotopic system to date fine-grained clay fractions associated with authigenic illite growth and remagnetization events (Tohver et al., 2008). Similarly, the Rb-Sr isotopic system has been applied to dating authigenic illite (e.g., Morton, 1985). While both methods have proven effective, they were traditionally used on powdered rock samples, which often contain a mixture of primary and post-depositional signatures. Recent advancements in laser ablation inductively coupled plasma mass spectrometry (LA-ICP-MS) now enable in situ mineral dating. Unlike bulk rock analyses, laser ablation allows precise targeting of specific micrometer-scale mineral fabrics, making it possible to distinguish and directly date later diagenetic alterations among primary depositional components. This approach has facilitated the accurate dating of diagenetic events in ancient rocks, including the authigenic growth of illite through reverse weathering (e.g., Subarkah et al., 2022; Zack and Hogmalm, 2016), and offers significant potential for dating remagnetization events.

6. Conclusions

This study underscores the power of integrating paleomagnetic and geochemical data with statistical learning techniques to unravel complex geological processes. Our findings reveal that the Ediacaran Itapucumi Group in Paraguay has undergone pervasive remagnetization. Stepwise demagnetization of the natural remanent magnetization (NRM) identified two distinct magnetic components: component A, a Cambro-Ordovician component hosted by magnetite, and component B, a Cretaceous or younger component associated with hematite. Our characterization of the magnetite hosting component A reveals it to be authigenic, and we quantify its abundance and contribution to the NRM via frequency-dependent susceptibility (X_{FV}).

Building on the fact that X_{FV} precisely measures the intensity of remagnetization, we investigated whether a dataset constructed from geochemical data could accurately predict this parameter. Using a Random

Forest regressor trained on geochemical data, we successfully predicted X_{FV} values, capturing the growth of fine-grained magnetite. Feature importance analysis from the Random Forest model identified K, Rb, and the K/Al ratio as the most significant predictors of X_{FV}. These findings highlight the pivotal role of clay authigenesis, with the K/Al ratio serving as a well-established proxy for illitization (van de Kamp, 2016).

Collectively, our results strongly suggest that authigenic magnetite growth was driven by Fe release during clay diagenesis in a geochemically closed system. This study demonstrates the utility of combining geochemical proxies and statistical learning to enhance our understanding of diagenetic processes and remagnetization, and opens new avenues toward the direct dating of such events.

CRediT authorship contribution statement

L.C. Gallo: Writing – original draft, Visualization, Validation, Supervision, Software, Project administration, Methodology, Investigation, Formal analysis, Data curation, Conceptualization. **M. Domeier:** Writing – review & editing, Writing – original draft, Validation, Supervision, Project administration, Investigation, Funding acquisition, Conceptualization. **P.Y. Antonio:** Writing – review & editing, Validation, Investigation, Data curation. **F. Sapienza:** Writing – review & editing, Validation, Software, Investigation. **A. Rapalini:** Writing – review & editing, Validation, Data curation. **E. Font:** Writing – review & editing, Validation, Data curation. **T. Adatte:** Writing – review & editing, Validation, Data curation. **R.I.F. Trindade:** Validation, Data curation. **F. Temporim:** Validation, Data curation. **J. Tonti-Filippini:** Writing – review & editing, Validation. **P. Silkoset:** Validation, Data curation. **L. Warren:** Writing – review & editing, Validation, Investigation, Funding acquisition, Data curation.

Declaration of competing interest

The authors declare that they have no known competing financial interests or personal relationships that could have appeared to influence the work reported in this paper.

Acknowledgements

This work was supported by the Research Council of Norway (RCN), through RCN's Centres of Excellence funding scheme, project 332523 (Centre for Planetary Habitability, University of Oslo), and from the European Research Council (ERC) under the European Union's Horizon 2020 research and innovation program (Grant agreement No. 101043844). LVW thanks FAPESP for the grant number 2023/14578-6. We thank Mark Dekkers and an anonymous reviewer for their thoughtful reviews of the manuscript, and we also appreciate the careful editorial handling by Huiming Bao.

Appendix A. Supplementary material

Supplementary material related to this article can be found online at https://doi.org/10.1016/j.epsl.2025.119390.

Data availability

The raw paleomagnetic measurements and directions are deposited in the Magnetics Information Consortium (MagIC) Database at earthref.org/MagIC/20337 (Gallo et al., 2025). All analyses and their associated code are available in the GitHub repository accompanying this paper (https://github.com/LenGallo/Gallo-etal-2025_Statistical-Learning-Remagnetizations), which is also archived in Zenodo (https://doi.org/10.5281/zenodo.15260555). The interactive digital outcrop models are available on Sketchfab: https://skfb.ly/pwrrC (TG01 Outcrop) and https://skfb.ly/pwrrp (TG02 Outcrop). Additional analysis was performed using PmagPy (Tauxe et al., 2016) and Scikit-learn (Pedregosa et al., 2011).

References

Adatte, T., Stinnesbeck, W., Keller, G., Ryder, G., Fastovsky, D., 1996. Lithostratigraphic and mineralogic correlations of near k/t boundary clastic sediments in northeastern Mexico: implications for origin and nature of deposition. Geol. Soc. Am. Spec. Pap. 307, e226.

Bayon, G., Bindeman, I.N., Trinquier, A., Retallack, G.J., Bekker, A., 2022. Long-term evolution of terrestrial weathering and its link to Earth's oxygenation. Earth Planet. Sci. Lett. 584, 117490.

Bayon, G., Freslon, N., Germain, Y., Bindeman, I.N., Trinquier, A., Barrat, J.A., 2021. A global survey of radiogenic strontium isotopes in river sediments. Chem. Geol. 559, 119958.

Beucher, S., Meyer, F., 2018. The morphological approach to segmentation: the watershed transformation. In: Mathematical Morphology in Image Processing. CRC Press, pp. 433–481.

Boles, J.R., Franks, S.G., 1979. Clay diagenesis in Wilcox sandstones of Southwest Texas; implications of smectite diagenesis on sandstone cementation. J. Sediment. Res. 49, 55–70.

Breiman, L., 2001. Using iterated bagging to debias regressions. Mach. Learn. 45, 261–277.

Brenner, A.R., Fu, R.R., Kylander-Clark, A.R., Hudak, G.J., Foley, B.J., 2022. Plate motion and a dipolar geomagnetic field at 3.25 GA. Proc. Natl. Acad. Sci. 119, e2210258119.

Collinson, D., 1974. The role of pigment and specularite in the remanent magnetism of red sandstones. Geophys. J. Int. 38, 253–264.

Dearing, J.A., Dann, R., Hay, K., Lees, J., Loveland, P., Maher, B.A., O'grady, K., 1996. Frequency-dependent susceptibility measurements of environmental materials. Geophys. J. Int. 124, 228–240.

Domeier, M., Robert, B., Meert, J.G., Kulakov, E.V., McCausland, P.J., Trindade, R.I., Torsvik, T.H., 2023. The enduring ediacaran paleomagnetic enigma. Earth-Sci. Rev. 242, 104444.

Donardelli Bellon, U., Trindade, R.I.F., Williams, W., Galante, D., Sant'Anna, L.G., Pescarini, T., 2024. Clay minerals and continental-scale remagnetization: a case study of South American neoproterozoic carbonates. J. Geophys. Res., Solid Earth 129, e2023JB028538.

Dunlop, D.J., 1973. Theory of the magnetic viscosity of lunar and terrestrial rocks. Rev. Geophys. 11, 855–901.

Dunlop, D.J., Özdemir, Ö., 1993. Thermal demagnetization of vrm and ptrm of single domain magnetite: no evidence for anomalously high unblocking temperatures. Geophys. Res. Lett. 20, 1939–1942.

Enkin, R.J., Baker, J., Nourgaliev, D., Iassonov, P., Hamilton, T.S., 2007. Magnetic hysteresis parameters and day plot analysis to characterize diagenetic alteration in gas hydrate-bearing sediments. J. Geophys. Res., Solid Earth 112.

Font, E., Trindade, R.I.F.d., Nédélec, A., 2006. Remagnetization in bituminous limestones of the neoproterozoic araras group (Amazon craton): hydrocarbon maturation, burial diagenesis, or both? J. Geophys. Res., Solid Earth 111.

Gallo, L., Domeier, M., Antonio, P.Y., Sapienza, F., Rapalini, A., Font, E., Adatte, T., Trindade, R.I.F., Temporim, F., Tonti-Filippini, J., Silkoset, P., Warren, L., 2025. Unraveling remagnetization sources using statistical learning. Magnetics Information Consortium (MagIC). https://doi.org/10.7288/V4/MAGIC/20337.

Gernon, T.M., Hincks, T.K., Brune, S., Braun, J., Jones, S.M., Keir, D., Cunningham, A., Glerum, A., 2024. Coevolution of craton margins and interiors during continental break-up. Nature 632, 327–335.

Gerritsen, D., Vaes, B., van Hinsbergen, D.J., 2022. Influence of data filters on the position and precision of paleomagnetic poles: what is the optimal sampling strategy? Geochem. Geophys. Geosyst. 23, e2021GC010269.

Grinsztajn, L., Oyallon, E., Varoquaux, G., 2022. Why do tree-based models still outperform deep learning on typical tabular data? Adv. Neural Inf. Process. Syst. 35, 507–520.

Heslop, D., Roberts, A.P., 2016. Analyzing paleomagnetic data: to anchor or not to anchor? J. Geophys. Res., Solid Earth 121, 7742–7753.

Hoffman, J., Hower, J., 1979. Clay Mineral Assemblages as Low Grade Metamorphic Geothermometers: Application to the Thrust Faulted Disturbed Belt of Montana, USA.

Hower, J., Eslinger, E.V., Hower, M.E., Perry, E.A., 1976. Mechanism of burial metamorphism of argillaceous sediment: 1. Mineralogical and chemical evidence. Geol. Soc. Am. Bull. 87, 725–737.

Huang, W., Jackson, M.J., Dekkers, M.J., Zhang, Y., Zhang, B., Guo, Z., Dupont-Nivet, G., 2019. Challenges in isolating primary remanent magnetization from Tethyan carbonate rocks on the Tibetan Plateau: insight from remagnetized Upper Triassic limestones in the eastern Qiangtang block. Earth Planet. Sci. Lett. 523, 115695.

Jackson, M., 1990. Diagenetic sources of stable remanence in remagnetized Paleozoic cratonic carbonates: a rock magnetic study. J. Geophys. Res., Solid Earth 95, 2753–2761.

Jackson, M., McCabe, C., Ballard, M.M., Van der Voo, R., 1988. Magnetite authigenesis and diagenetic paleotemperatures across the northern Appalachian basin. Geology 16, 592–595.

Jackson, M., Swanson-Hysell, N.L., 2012. Rock magnetism of remagnetized carbonate rocks: another look. Geol. Soc. (Lond.) Spec. Publ. 371, 229–251.

van de Kamp, P.C., 2016. Potassium distribution and metasomatism in pelites and schists: how and when, relation to postdepositional events. J. Sediment. Res. 86, 683–711.
Katz, B., Elmore, R., Cogoini, M., Ferry, S., 1998. Widespread chemical remagnetization: orogenic fluids or burial diagenesis of clays? Geology 26, 603–606.
Kent, D.V., 1985. Thermoviscous remagnetization in some Appalachian limestones. Geophys. Res. Lett. 12, 805–808.
Kirschvink, J., 1980. The least-squares line and plane and the analysis of palaeomagnetic data. Geophys. J. Int. 62, 699–718.
Kubler, B., 1967. La cristallinite de i'illite et les zones tout a fait superieures de metamorphisme. In: Etages Tectoniques, Colloque de Neuchâtel 1966, A la Baconniere, pp. 105–121.
Liu, Q., Yu, Y., Torrent, J., Roberts, A.P., Pan, Y., Zhu, R., 2006. Characteristic low-temperature magnetic properties of aluminous goethite [α-(fe, al) ooh] explained. J. Geophys. Res., Solid Earth 111.
Lowrie, W., 1990. Identification of ferromagnetic minerals in a rock by coercivity and unblocking temperature properties. Geophys. Res. Lett. 17, 159–162.
Lu, G., McCabe, C., Hanor, J.S., Ferrell, R.E., 1991. A genetic link between remagnetization and potassic metasomatism in the Devonian Onondaga Formation, Northern Appalachian Basin. Geophys. Res. Lett. 18, 2047–2050.
Lundberg, S., 2017. A unified approach to interpreting model predictions. arXiv preprint arXiv:1705.07874.
Maxbauer, D.P., Feinberg, J.M., Fox, D.L., 2016. Max unmix: a web application for unmixing magnetic coercivity distributions. Comput. Geosci. 95, 140–145.
McCabe, C., Jackson, M., Saffer, B., 1989. Regional patterns of magnetite authigenesis in the Appalachian basin: implications for the mechanism of late Paleozoic remagnetization. J. Geophys. Res., Solid Earth 94, 10429–10443.
Meunier, A., Velde, B.D., 2013. Illite: Origins, Evolution and Metamorphism. Springer Science & Business Media.
Moore, D.M., Reynolds Jr., R.C., 1989. X-ray Diffraction and the Identification and Analysis of Clay Minerals.
Morton, J.P., 1985. Rb-sr dating of diagenesis and source age of clays in upper devonian black shales of Texas. Geol. Soc. Am. Bull. 96, 1043–1049.
Oliver, J., 1986. Fluids expelled tectonically from orogenic belts: their role in hydrocarbon migration and other geologic phenomena. Geology 14, 99–102.
Özdemir, Ö., Dunlop, D.J., 2010. Hallmarks of maghemitization in low-temperature remanence cycling of partially oxidized magnetite nanoparticles. J. Geophys. Res., Solid Earth 115.
Özdemir, Ö., Dunlop, D.J., 2014. Hysteresis and coercivity of hematite. J. Geophys. Res., Solid Earth 119, 2582–2594.
Pedregosa, F., Varoquaux, G., Gramfort, A., Michel, V., Thirion, B., Grisel, O., Blondel, M., Prettenhofer, P., Weiss, R., Dubourg, V., Vanderplas, J., Passos, A., Cournapeau, D., Brucher, M., Perrot, M., Duchesnay, E., 2011. Scikit-learn: machine learning in Python. J. Mach. Learn. Res. 12, 2825–2830.
de la Peña, F., Ostasevicius, T., Fauske, V.T., Burdet, P., Jokubauskas, P., Nord, M., Sarahan, M., Prestat, E., Johnstone, D.N., Taillon, J., et al., 2017. Electron microscopy (big and small) data analysis with the open source software package hyperspy. Microsc. Microanal. 23, 214–215.
Pescarini, T., Trindade, R.I., Hoffman, P.F., Gomes Sant'Anna, L., 2024. Paleomagnetic investigation of the basal Maieberg Formation (Namibia) cap carbonate sequence (635 Ma): implications for Snowball Earth postglacial dynamics. Geol. Soc. Am. Bull. 136, 4775–4797.
Pisarevsky, S., Li, Z., Tetley, M., Liu, Y., Beardmore, J., 2022. An updated internet-based global paleomagnetic database. Earth-Sci. Rev. 235, 104258.
Pullaiah, G., Irving, E., Buchan, K., Dunlop, D., 1975. Magnetization changes caused by burial and uplift. Earth Planet. Sci. Lett. 28, 133–143.
Rasmussen, B., Muhling, J.R., 2019. Syn-tectonic hematite growth in Paleoproterozoic Stirling Range "red beds", Albany-Fraser Orogen, Australia: evidence for oxidation during late-stage orogenic uplift. Precambrian Res. 321, 54–63.
Roberts, A.P., Florindo, F., Chang, L., Heslop, D., Jovane, L., Larrasoaña, J.C., 2013. Magnetic properties of pelagic marine carbonates. Earth-Sci. Rev. 127, 111–139.
Roberts, A.P., Heslop, D., Zhao, X., Pike, C.R., 2014. Understanding fine magnetic particle systems through use of first-order reversal curve diagrams. Rev. Geophys. 52, 557–602.
Saigal, G.C., Morad, S., Bjorlykke, K., Egeberg, P.K., Aagaard, P., 1988. Diagenetic albitization of detrital K-feldspar in Jurassic, Lower Cretaceous, and Tertiary clastic reservoir rocks from offshore Norway; I, textures and origin. J. Sediment. Res. 58, 1003–1013.
Sapienza, F., Gallo, L.C., Zhang, Y., Vaes, B., Domeier, M., Swanson-Hysell, N.L., 2023. Quantitative analysis of paleomagnetic sampling strategies. J. Geophys. Res., Solid Earth 128, e2023JB027211.
Somoza, R., Zaffarana, C.B., 2008. Mid-Cretaceous polar standstill of South America, motion of the Atlantic hotspots and the birth of the Andean cordillera. Earth Planet. Sci. Lett. 271, 267–277.
Subarkah, D., Blades, M.L., Collins, A.S., Farkaš, J., Gilbert, S., Löhr, S.C., Redaa, A., Cassidy, E., Zack, T., 2022. Unraveling the histories of proterozoic shales through in situ rb-sr dating and trace element laser ablation analysis. Geology 50, 66–70.
Tarduno, J.A., 1992. Magnetic susceptibility cyclicity and magnetic dissolution in Cretaceous limestones of the southern Alps (Italy). Geophys. Res. Lett. 19, 1515–1518.
Tauxe, L., Shaar, R., Jonestrask, L., Swanson-Hysell, N., Minnett, R., Koppers, A., Constable, C., Jarboe, N., Gaastra, K., Fairchild, L., 2016. Pmagpy: software package for paleomagnetic data analysis and a bridge to the magnetics information consortium (magic) database. Geochem. Geophys. Geosyst. 17, 2450–2463.
Tauxe, L., Watson, G., 1994. The fold test: an eigen analysis approach. Earth Planet. Sci. Lett. 122, 331–341.
Tohver, E., Trindade, R.I.F.d., Solum, J., Hall, C.M., Riccomini, C., Nogueira, A., 2010. Closing the Clymene ocean and bending a Brasiliano belt: evidence for the Cambrian formation of Gondwana, southeast Amazon craton. Geology 38, 267–270.
Tohver, E., Weil, A., Solum, J., Hall, C., 2008. Direct dating of carbonate remagnetization by 40ar/39ar analysis of the smectite–illite transformation. Earth Planet. Sci. Lett. 274, 524–530.
Torsvik, Trond H., Van der Voo, Rob, Preeden, Ulla, Mac Niocaill, Conall, Steinberger, Bernhard, Doubrovine, Pavel V., Van Hinsbergen, Douwe J.J., Domeier, Mathew, Gaina, Carmen, Tohver, Eric, et al., 2012. Phanerozoic polar wander, palaeogeography and dynamics. Earth-Sci. Rev. 114 (3–4), 325–368.
Trindade, R.I., D'Agrella-Filho, M.S., Babinski, M., Font, E., Neves, B.B.B., 2004. Paleomagnetism and geochronology of the Bebedouro cap carbonate: evidence for continental-scale Cambrian remagnetization in the São Francisco craton, Brazil. Precambrian Res. 128, 83–103.
Van Der Voo, R., Torsvik, T.H., 2012. The History of Remagnetization of Sedimentary Rocks: Deceptions, Developments and Discoveries. Special Publications, vol. 371. Geological Society, London, pp. 23–53.
Van Velzen, A., Zijderveld, J., 1995. Effects of weathering on single-domain magnetite in early Pliocene marine marls. Geophys. J. Int. 121, 267–278.
Walker, T.R., Larson, E.E., Hoblitt, R.P., 1981. Nature and origin of hematite in the Moenkopi Formation (Triassic), Colorado Plateau: a contribution to the origin of magnetism in red beds. J. Geophys. Res., Solid Earth 86, 317–333.
Warren, L.V., Freitas, B., Riccomini, C., Boggiani, P.C., Quaglio, F., Simões, M., Fairchild, T.R., Giorgioni, M., Gaucher, C., Poire, D.G., et al., 2019. Sedimentary evolution and tectonic setting of the Itapucumi Group, Ediacaran, northern Paraguay: from Rodinia break-up to West Gondwana amalgamation. Precambrian Res. 322, 99–121.
Warren, L.V., Inglez, L., Xiao, S., Buatois, L.A., Mángano, M.G., Okubo, J., Alessandretti, L., Simões, M.G., Riccomini, C., Antunes, G.C., et al., 2023. Evolutionary, paleoecological, and biostratigraphic implications of the Ediacaran-Cambrian interval in West Gondwana. Geol. Soc. Am. Bull. 135, 3102–3111.
Zack, T., Hogmalm, K.J., 2016. Laser ablation rb/sr dating by online chemical separation of rb and sr in an oxygen-filled reaction cell. Chem. Geol. 437, 120–133.